Original Article

Miniature Flexible Instrument with Fibre Bragg Grating-Based Triaxial Force Sensing for Intraoperative Gastric Endomicroscopy

ZHONGYUAN PING, TIANCI ZHANG, LUN GONG, CHI ZHANG,
and SIYANG ZUO [ORCID]

Key Laboratory of Mechanism Theory and Equipment Design of Ministry of Education, Tianjin University, Tianjin 300072,
China

Associate Editor Ka-Wai Kwok oversaw the review of this article.

Abstract—Optical biopsy methods, such as probe-based endomicroscopy, can be used to identify early-stage gastric cancer *in vivo*. However, it is difficult to scan a large area of the gastric mucosa for mosaicking during endoscopy. In this work, we propose a miniaturised flexible instrument based on contact-aided compliant mechanisms and fibre Bragg grating (FBG) sensing for intraoperative gastric endomicroscopy. The instrument has a compact design with an outer diameter of 2.7 mm, incorporating a central channel with a diameter of 1.9 mm for the endomicroscopic probe to pass through. Experimental results show that the instrument can achieve raster trajectory scanning over a large tissue surface with a positioning accuracy of 0.5 mm. The tip force sensor provides a 4.6 mN resolution for the axial force and 2.8 mN for transverse forces. Validation with random samples shows that the force sensor can provide consistent and accurate three-axis force detection. Endomicroscopic imaging experiments were conducted, and the flexible instrument performed no gap scanning (mosaicking area more than 3 mm^2) and contact force monitoring during scanning, demonstrating the potential of the system in clinical applications.

Keywords—Optical biopsy, Gastric cancer, Flexible instrument, Force sensing, Mosaicking.

INTRODUCTION

Gastric cancer (GC) is one of the leading causes of cancer-related deaths worldwide.[5] It was the fifth most frequently diagnosed cancer and the third most common cause of cancer death.[2] Symptoms often appear at a late stage, which contributes to poor prognosis.

Therefore, the early detection and diagnosis of gastric cancers are essential to significantly improve the five-year survival rate of patients (10% for advanced GC and 90% for early-stage GC[15]).

Endoscopy and endoscopic biopsy are the gold standard procedures for early gastric cancer screening. However, conventional white light endoscopy can only obtain macro images of gastric tissue, while pinch biopsies have disadvantages, such as delayed treatment, that result from the time-consuming and inaccurate diagnosis caused by sampling error, injury, and incremental cost.[23]

Probe-based confocal laser endomicroscopy (pCLE), which provides *in vivo* and *in situ* cellular-level imaging for real-time assessment of tissue pathology, offers the potential to decrease or even eliminate the need for some biopsies to directly guide the treatment of circumscribed lesions.[23] pCLE has been most extensively applied to detect diseases in the lung[17] bladder,[19] and stomach.[11] pCLE has several advantages, including the combination with a standard endoscope using the instrumental channel.

Although preliminary clinical trials have demonstrated the potential of this technique, a major limitation of pCLE is that its field-of-view (FoV) tends to be smaller than the histology section—typically less than 0.5 mm in diameter for a high-resolution probe—which makes it difficult to provide sufficient visual information on the tissue for clinicians. Manual manipulation of the probe also makes it difficult to operate precisely. To overcome these problems and cover a large area of the tissue to be surveyed, it is necessary to stitch together individual image frames to form a local panoramic image. Some robotic scanning

---

Address correspondence to Siyang Zuo, Key Laboratory of Mechanism Theory and Equipment Design of Ministry of Education, Tianjin University, Tianjin 300072, China. Electronic mail: siyang_zuo@tju.edu.cn

devices[6,7,24,28] and mosaicking algorithms, including both real-time and offline processing approaches,[8,22] have been developed. However, these rigid devices can only be used in specific minimally invasive surgeries and are not applicable to the gastrointestinal (GI) tract.

A tendon-driven continuum robot[3] is the ideal choice for real-time gastric endomicroscopy as it is both compact and dexterous. It can also provide adequate power through a narrow, tortuous endoscope working channel, which allows the actuators to be located at a safe distance from the patient. Compared with traditional articulated continuum manipulators,[10,18] compliant mechanisms based on a Nitinol tube[12,14,20,26] have significant advantages, such as less assembly, self-backbone and no lubrication requirements. A multi-cavity tube is commonly used as the passive flexible shaft to be combined with continuum robot.[18] Compared with traditional multi-cavity tube (difficulties in thin wall manufacturing), the notched Nitinol tube has a larger inner lumen and higher material strength. The typical compliant mechanism is rectangular notched tube (contained chamfer or fillet types etc.).[12,14,20,26] However, this type of compliant mechanisms also has disadvantages, such as no fixed pivot, and poor tensile and torsional strength due to slight flexure hinge. Therefore, a new compliant mechanism must be developed.

During the pCLE scanning, the appropriate contact force between probe and tissue is important for imaging quality. Large contact force causes large tissue deformation, which may change the microstructure of the tissue and affect the smoothness of the scanning. On the other hand, if the contact force is too small, the images will be blurred or lost. Hence, lacking of force information could also cause clinical risk such as perforation of the GI tract. To achieve quality mosaics and safe endoluminal intervention, the contact force between human tissues and the imaging probe needs to be monitored. Several smart instruments incorporate adaptive force sensing.[13,16,25] Latt et al.[13] developed handheld one-degree-of-freedom (1-DOF) active force-controlled instruments. Load cells were used to sense forces applied axially to the tissue that can maintain consistent tissue contact at 100 mN. A cable-driven parallel manipulator with force sensing for high-accuracy tissue endomicroscopy was developed by Miyashita et al.[16] The axial contact force was calculated using the cable tension measured by the load cells. Wisanuve et al.[25] proposed a cooperatively controlled robotic manipulator that can achieve 3-DOF force sensing by a multi-axis force sensor to perform local mosaics. Although force sensing was achieved by these researchers,[13,16,25] these works are difficult to adapt for the GI tract using conventional load cells.

Force sensing, based on fibre Bragg grating (FBG) sensors, is a promising approach to detect the tool-tissue interaction force. The advantages of FBG sensors include their small dimensions, high sensitivity, low cost, sterilizability, biocompatibility etc. Wang et al.[24] developed a handheld robotic scanning device with 1-DOF force-sensing based on an FBG sensor. This instrument was used for intraoperative thyroid gland endomicroscopy. He et al.[9] developed a sub-millimetre 3-DOF force-sensing instrument with an integrated FBG for retinal microsurgery. A handheld micromanipulator with tool-tissue interaction force-sensing was also developed by Balicki et al.[1] Although force-sensing instruments were achieved, these studies[1,9,24] were targeted at applications for rigid surgical devices.

In this study, we propose a flexible instrument based on a contact-aided compliant mechanism (CCM) and FBG sensing for intraoperative gastric endomicroscopy (Fig. 1). The proposed instrument is compatible with a standard endoscope or other operating platforms of natural orifice transluminal endoscopic surgery.

The main design features of the instrument include the following: (1) a specially designed CCM for the whole instrument structure to improve the mechanical performance, such as torsional and tensile strength, and more perfect deflection around the centroid compared with a typical compliant mechanism based on a rectangular notch joint; (2) a three-axis FBG-based force-sensing mechanism consisting of a Nitinol tube with flexure cut by laser micromachining, which allows millinewton-level force sensing; and (3) a larger internal working channel space for the imaging probe to pass through and an outer diameter smaller than traditional multi-cavity tubes. To the best of our knowl-
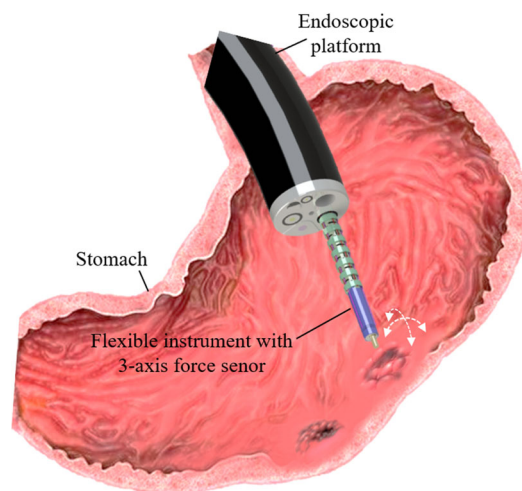

FIGURE 1. The application scenarios of the proposed instrument.

edge, this is the first work to simultaneously achieve no-gap raster trajectory endomicroscopic scanning and 3-DOF contact force monitoring using a flexible instrument. The remainder of this paper presents the detailed design considerations and mechanical performance validation of the instrument. The mosaicking results from *ex vivo* porcine gastric tissue are presented to demonstrate that the instrument can achieve large-area scanning, endomicroscopic image mosaicking, and 3-DOF contact force monitoring.

MATERIALS AND METHODS

Design Requirements

The instrument is intended to be used through the work channel of an endoscopic platform. Thus, its outer diameter should be less than the inner diameter of the work channel (typical 2.8–3.2 mm). Length of the instrument should match the endoscopic platform (typically > 600 mm in prototype).[21,27] The process of the scanning needs three DOFs. One of them is axial linear motion used to make imaging probe approach the tissue and the other two are bending DOFs used to achieve surface scanning. Contact force between tissue and imaging probe is generally 50–100 mN.[16,24] The requirement of scanning area is more than 3 mm².[6,7] The defined parameters are summarized in Table 1. The flexible instrument should consist of two parts: a flexible insertion unit and an actuation unit. Detailed design considerations are presented in the following sections.

Flexible Insertion Unit

The flexible insertion unit includes a passive flexible shaft and scanning section. The length of each section is shown in Fig. 2. The whole structure of the unit is cut by laser micromachining from Nitinol tubes (Peiertech Inc., China) to form a series of contact-aided compliant mechanisms (CCMs). The CCMs include flexure hinge and contact-aided structures. These compliant joints are arranged equidistantly in two orthogonal planes. The outer diameter of the Nitinol

TABLE 1. Design requirements

Parameter	Value
Instrument diameter	≤ 3 mm
Instrument length	≥ 600 mm
Force range	≤ 50 mN
Degree of freedom	2-DOFs bending and 1-DOF axial motion
Scanning area	≥ 3 mm²

tube was 2.2 mm. The scanning section and flexible shaft were fabricated in an integrated manner. The maximum strain of the Nitinol material should be less than the elastic strain limit. Generally, the elastic strain limit of the Nitinol material is 6%–8%. A conservative range of 3%–4% was selected in this design. The detailed parameters of the mechanism are summarised in Table 2.

w_1 and w_2 are the tangent widths of the curved flexure hinges in the scanning section and flexible shaft, respectively, as shown in Fig. 2.

The scanning section can be actuated by wires bending from $-105°$ to $+105°$ in four directions (up/down and left/right). The Nitinol actuation wires are 0.1 mm in diameter.

The wire-guide disks were assembled on the outer wall of the tube. The spaces between the wire-guide disks are 2 and 10 mm in the scanning section and flexible shaft, respectively.

Force-Sensing Unit

The three-axis force-sensing unit includes the Nitinol tube with flexure and four FBG sensors (marked in purple in Fig. 2—transparent and top views). An optical sensing interrogator was used to monitor the wavelength variations of the FBG sensors, which has a resolution of 0.001 nm and four channels (maximum sample frequency: 100 Hz). The Bragg wavelength changes were read by a computer from an interrogator (si-155, Micron Optics Inc., USA, GA). To increase the axial force sensitivity, the stiffness of the Nitinol tube should be reduced by creating a flexure segment. The flexure was cut into multi-layer parallel slits by laser micromachining. Its 2D unfolded pattern with key dimensions is shown in Fig. 2.

The wire-guide disks, with outer diameter of 2.7 mm, were cut into five through-holes and three slits on the end face. As shown in Fig. 2—top view, four holes were fabricated symmetrically along the circumference used to guide four actuation wires. The big hole at the centre was fit with the Nitinol tube. Three slits were cut at 120° intervals to guide the outer FBG sensors 1–3 and the diameter of the three slits is 0.15 mm (Fig. 2). The imaging probe and FBG 4 are inserted through the central channel (⌀1.9 mm) of the Nitinol tube. The tips of FBG sensor 4 and the imaging probe were eccentrically fixed to the top disk of the force-sensing unit. The grating region tail of FBG sensor 4 was fixed to the end half-circular disk (Fig. 2—transparent view). The outer diameter of the FBG was 100 μm (length of FBG segment: 5 mm, centre Bragg wavelength: 1545 nm; Ske, Beijing, China). The inner FBG sensor 4 monitors the strain variations that result from axial
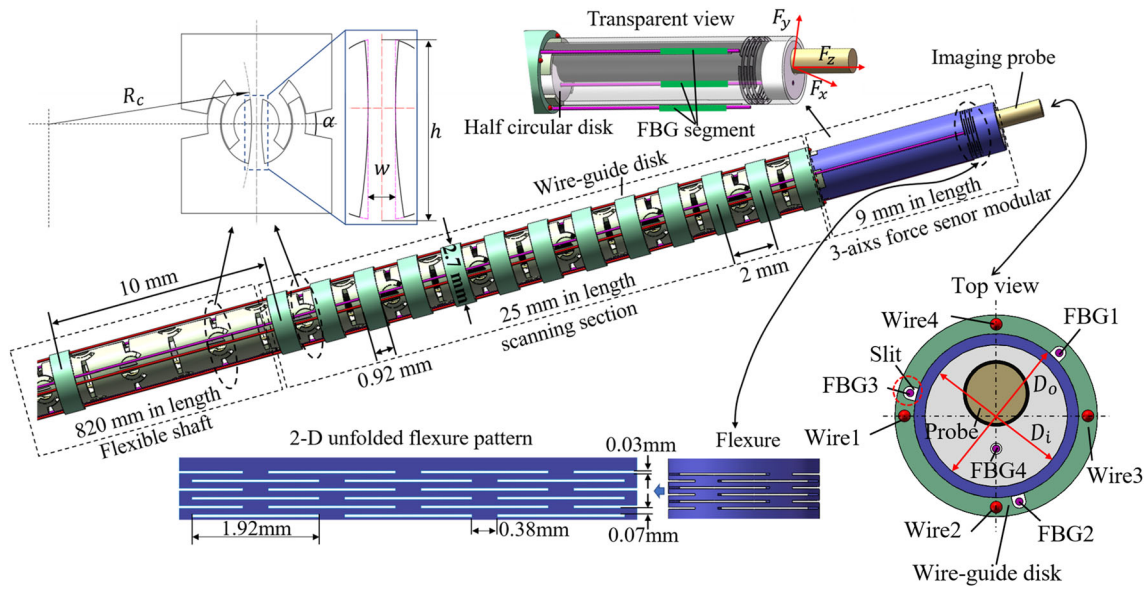
FIGURE 2. The design of the flexible robotic scanning instrument with the FBG-based three-axis force sensor at the tip.

TABLE 2. Parameter selection summary.

Joint parameter	Value
Tube outer diameter D_o	2.2 mm
Tube inner diameter D_i	1.9 mm
Flexure hinge width w_1	0.18 mm
Flexure hinge width w_2	0.2 mm
Radius of curvature R_c	7 mm
Flexure hinge height h	0.86 mm
Number of joints n	7 in each bending plane
Bending directions	4
Maximum bending angle of each joint α	15°

forces, while the outer FBG sensors 1–3 measure the transverse forces.

Owing to the eccentric configuration, the inner FBG sensor was not completely decoupled from transverse forces. Thus, a non-linear model was investigated.

Finite Element Analysis

Finite element analysis (FEA) is used to evaluate the maximum strain of the compliant mechanism. The parameters of the Nitinol constitutive model were provided by the manufacturer (Peiertech Inc., China). The Young's modulus is 70 GPa and the weight percentage of nickel is 55.5%. The starting and final stress values for the forward phase and reverse phase transformations are 342 and 443 MPa, and 187 and 120 MPa, respectively.

As shown in Figs. 3a and 3c, automatic meshing was used for the global mesh. Local mesh (0.025 mm)

refinement of the flexure hinges and force-sensing flexure were used to obtain high solution accuracy. Fixed supports were applied to the underside of the two models. Loads were applied perpendicular to the end face of the joint to simulate the wire actuation and to bend it at 15°, as shown in Fig. 3a. Frictional contacts were selected with a friction coefficient of 0.1 between contact-aided structures. As shown in Fig. 3c, F (10 mN) was applied to the end face of the force-sensing unit model to simulate the contact force.

The FEA results (Fig. 3b) show that the maximum strains along the white dotted line in the flexure hinge are 3.5 and 4%, respectively, when the bending angle is $\alpha = 15°$. Both results are in accordance with the desired design value range (3%–4%).

Minimum changes of strain can be detected by FBG sensors is less than 1 μ strain. The maximum deformation of the force-sensing unit is 1×10^{-4} mm (Fig. 3c). The length of the force-sensing unit is 9 mm. Therefore, the maximum strain converted to FBG is approximately $1 \times 10^{-4}/9 = 1.1 \times 10^{-5} = 11 \, \mu$ strain, which satisfies our design requirements.

Force Calculation Algorithm

The Bragg wavelength variation due to strain and temperature can be expressed as

$$\Delta\lambda_i = k_{\varepsilon i}\Delta\varepsilon_i + k_{\Delta T}\Delta T, \quad i = 1, 2, 3, 4 \qquad (1)$$

where $\Delta\lambda_i$ denotes the Bragg wavelength variation in the FBG sensor i; $\Delta\varepsilon_i$ is the strain variation of the FBG sensor i; ΔT represents the changes in temperature; and
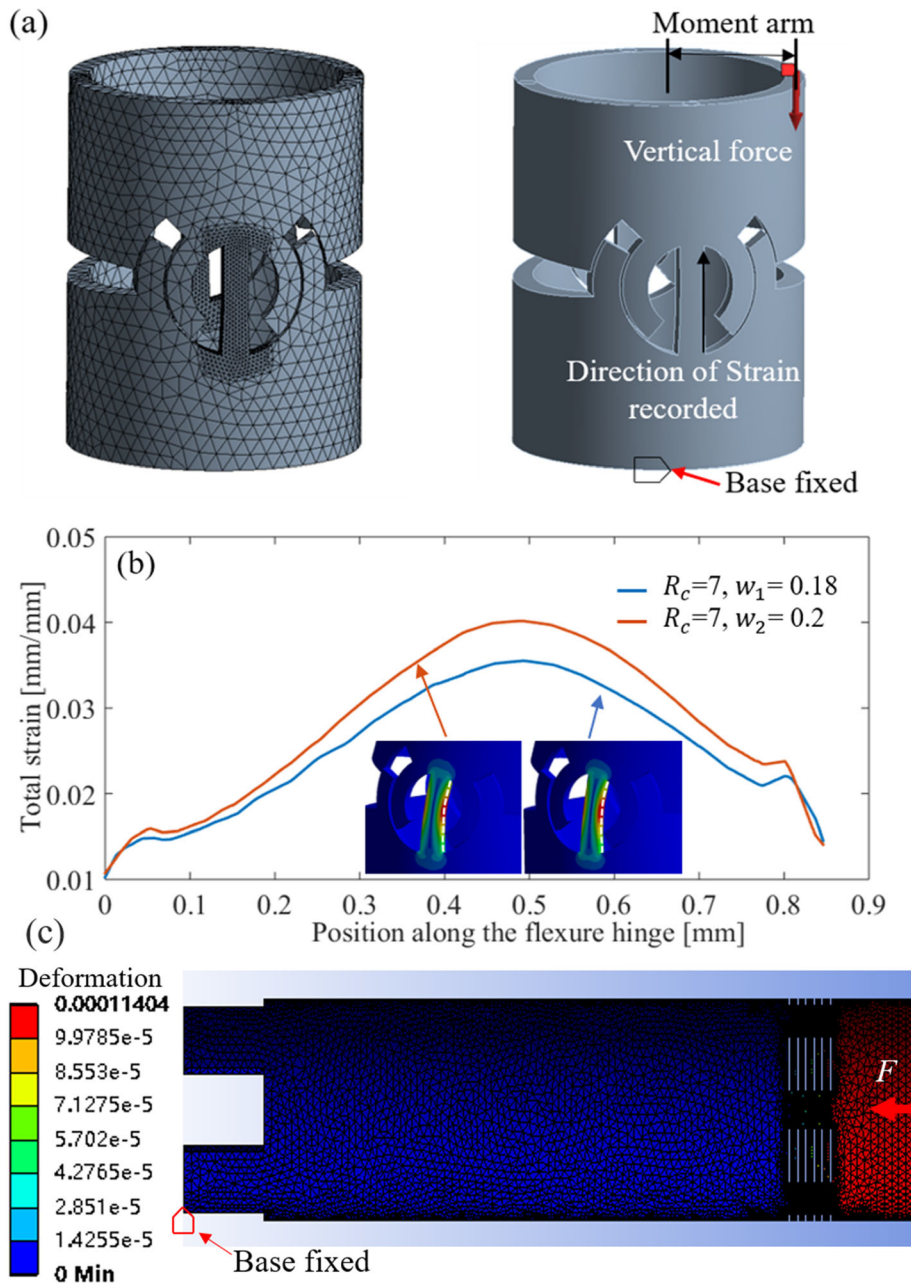
FIGURE 3. Modelling and FEA results. (a) Model mesh, constraints, and boundary condition. (b) Strain variations. (c) Deformation results of the force-sensing unit.

$k_{\varepsilon i}$ and $k_{\Delta T}$ are constant coefficients associated with the strain and temperature, respectively.

A proven method in Ref. 9 was used to remove the noise of the Bragg wavelength variation resulting from the axial strain and temperature component by subtracting the mean value from each wavelength variation. The method is defined as

$$\Delta s_i = \Delta\lambda_i - \frac{1}{3}k\sum_{i=1}^{3}\Delta\lambda_i, i = 1, 2, 3, 4 \qquad (2)$$

where Δs_i represents the differential mode in the FBG sensor i, and k denotes the slope of the linear dependence between the inner FBG sensor 4 and the outer FBG sensors 1–3. The strain ε on the surface of the Nitinol tube is proportional to the applied force.[9] Thus, a linear relationship between Δs and the applied force can be obtained in the corresponding x-y coordinates as shown below:

$$\begin{bmatrix} F_x \\ F_y \end{bmatrix} = K_t \begin{bmatrix} \Delta s_1 \\ \Delta s_2 \\ \Delta s_3 \end{bmatrix} \tag{3}$$

where $[F_x F_y]^T$ denotes the estimated lateral force components applied at the tool tip, and $[\Delta s_1 \Delta s_2 \Delta s_3]^T$ denotes the differential modes of the three outer FBG sensors. K_t is a 2×3 mapping coefficient matrix calculated by a calibration experiment.

The inner FBG sensor is not at the centre of the tube. Hence, the relationship between the differential mode wavelength variations of the FBG sensors and the axial force is non-linear. To decouple the axial force from the lateral forces, we used an artificial neural network (ANN) for regression. In this method, the ANN is a two-layer feed-forward network. The inputs are the differential mode wavelength variations of the four fibres, while the output is the applied axial force. The first layer includes 10 sigmoid neurons, and the second layer contains a linear neuron. Once the network is properly trained, it can be used to calculate the axial force.

Actuation Unit

The compact actuation unit is shown in Fig. 4, which consists of five sets of linear actuators. Stepper motors (AM2224R3, Faulhaber SA, Germany) equipped with lead screws (M3 × 100 T, 0.5 mm pitch) and magnetic encoders (AE 23B8, Faulhaber SA, Germany) were entailed in these linear actuators. Stepper drivers (MCST3601, Faulhaber SA, Germany) were used to drive the motors. The top four motors (motors 1–4) were used to generate the linear motion

of four actuation wires. Another motor (motor 5, transparent part in Fig. 4) was used to generate the linear motion of the whole flexible instrument to make contact with the target tissues. The linear actuators provide a stroke of 80 mm with a theoretical position resolution of less than 0.01 mm. Four sets of pulleys between the four sets of linear actuators and flexible insertion unit were used to guide and apply tension to the actuation wires.

Kinematics, Trajectory, and Control

Constant curvature assumption is frequently used for predicting the relationship between the bending angle of the continuum mechanism and the displacement of the actuation wires. If this relationship is known, then we can obtain the relationship between the arc length of the instrument tip and the displacement of the actuation wires. However, the general kinematic modelling method fails to accurately predict the bending motion of this long and flexible instrument. The motion errors are mainly caused by assembly errors and friction. Therefore, a statistical method was employed to improve the motion accuracy. A raster pattern was selected as the target trajectory, which includes long and short arcs, as shown in Fig. 5a. To evaluate the scanning arc length, we simplified the arc as a circular arc, as shown in Fig. 5b.

The relationship between the actuation wire displacement (x_i) and the bending angle (θ_i) is $\theta_i = f(x_i)$, $i = 1, 2$. The function is defined by the experimental method described in "Calibration and Validation of Force Sensor" section. The actuation wire displacement x_i is given by
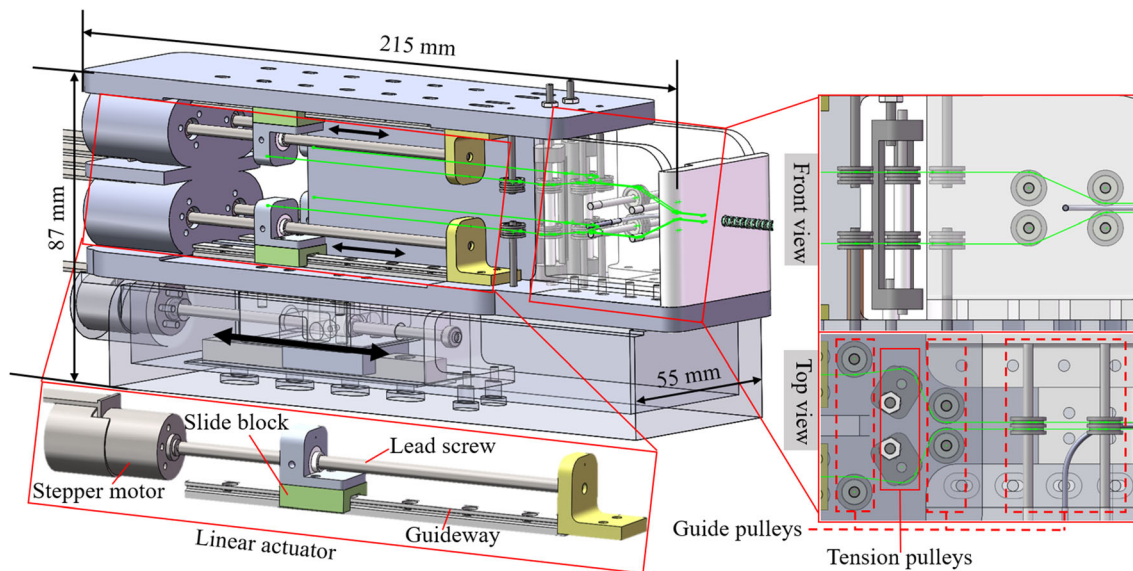
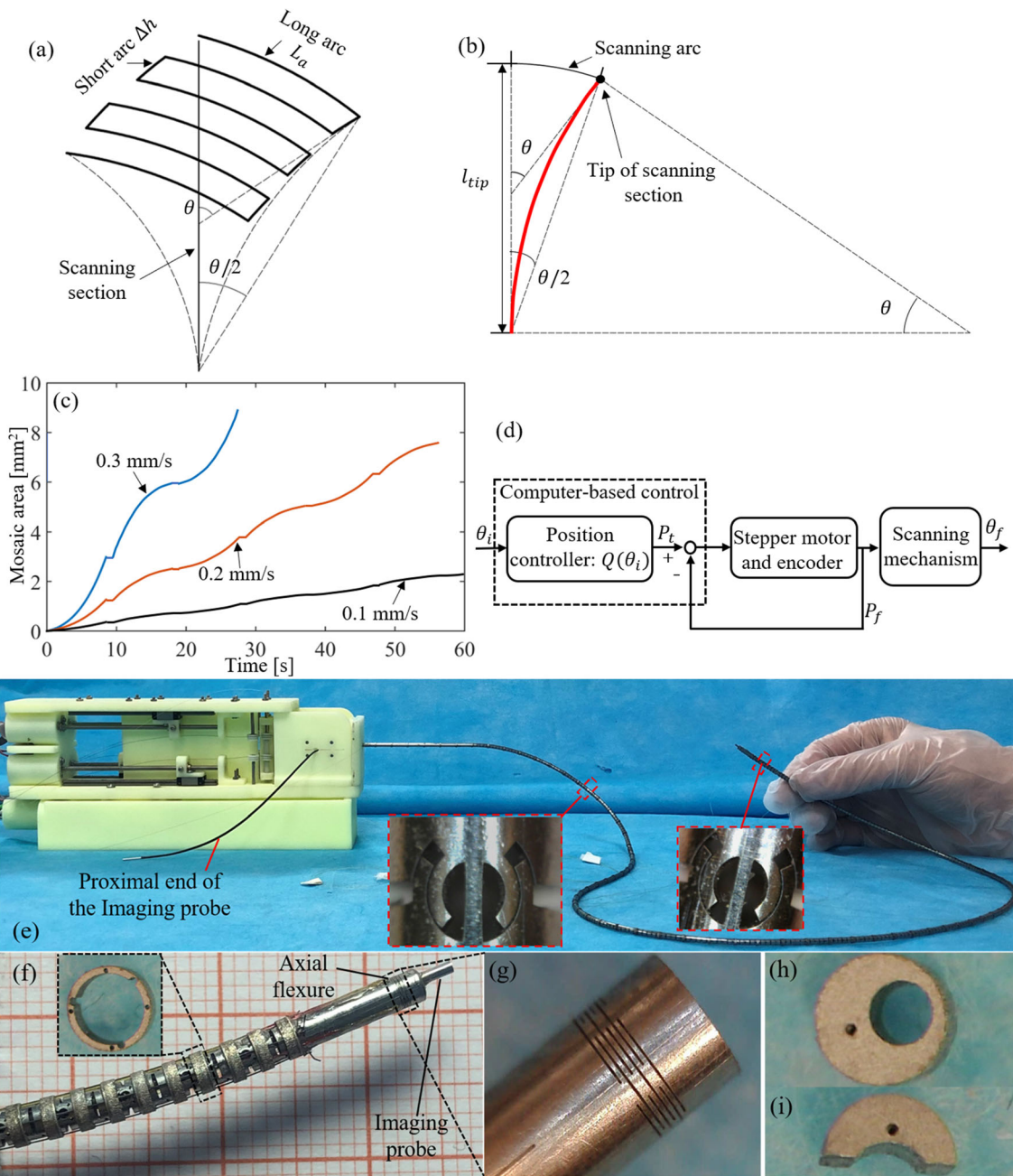

FIGURE 4. The design of actuation unit.

FIGURE 5. (a) Raster trajectory. (b) Simplified model for calculating scanning arc length. (c) Scanning time vs. mosaic area (d) Control diagram for bending. (e) Overall structure. (f) Scanning section tip. (g) Local enlarged picture of the force-sensing flexure. (h) The top disk. (i) The end half-circular disk.

$$x_1 = \frac{W_{mj} \cdot t_1 \cdot P}{60} \qquad (4)$$

where t_1 is the scanning time for the long arc, P is the pitch of the lead screw, and W_{mj} is the rotation frequency of the stepper motor j ($j = 1, 3$). When driving the instrument, motors 1 and 3 always work together. If one is responsible for pulling its corresponding

actuation wire, then the other one releases the wire at the same speed at the same time, and vice versa.

The length of the long arc L_{la} at a given time is related to the range of the bending angle θ_1. The simplified model for calculating the scanning arc length is shown in Fig. 5b, and expressed as

$$L_{la} = l_{tip} \cdot \frac{\theta_1}{2} = \frac{1}{2} l_{tip} \cdot f\left(\frac{W_{mj} \cdot t_1 \cdot P}{60}\right) \qquad (5)$$

where the l_{tip} is the length of the instrument tip for scanning.

To complete the gapless mosaicking, the length of the short arc L_{sa} must satisfy the following expression:

$$L_{sa} = l_{tip} \cdot \frac{1}{2} f \left(\frac{W_{mk} \cdot t_2 \cdot P}{60} \right) = \Delta h \leq FoV \qquad (6)$$

where t_2 is the scanning time for the short arc, W_{mk} is the rotation frequency of stepper motor 2 or 4, and Δh is the spacing between two adjacent long arcs.

If $\Delta h = FoV$, then the approximate mosaic area is given by Eq. (7).

$$S = L_{la} \cdot \Delta h \qquad (7)$$

The relationship between the mosaic area and scanning time is plotted in Fig. 5c. The different velocities represent the velocities of the actuation wire in a long arc stroke.

The velocity of the actuation wire is 0.5 mm/s in the short arc section. The initial status of the scanning section is straight without bending. To trade-off the smooth scanning and high efficiency, the scanning velocity of 0.2 mm/s was selected.

The control diagram is shown in Fig. 5d, which is applicable to 2-DOF scanning (long and short arc directions). In this diagram, θ_i represents the input target bending angle; $Q(\theta_i)$ is the solution of the actuation wire displacement model; P_t is the target linear displacement of the actuation wire; P_f denotes the corresponding actual displacement; and θ_f is the actual bending angle of the scanning section.

Fabrication and Assembly of the Prototype

The prototype is shown in Figs. 5e and 5f. It has an outer diameter of 2.7 mm, incorporating a central 1.9 mm diameter hollow channel for a leached fibre bundle to pass through. The instrument has a total length of 854 mm, while the length of the bending tip is 25 mm. The Nitinol tube and wire guide disks were cut using a three-axis precision laser machine (Yunco Precision Industrial Technology Inc., China; positioning accuracy: ± 3 μm). One benefit of the proposed flexible insertion unit design is the relative simplicity of fabricating the insertion part to an arbitrary length. Wire guide disks can provide guidance for the actuation wire and ensure motion decoupling in two orthogonal planes (Fig. 5f). The kerf width between the contact-aided structures is approximately 20 μm. In the assembly process, a high-strength medical adhesive (Loctite 4013, Henkel Inc., Germany) was used to bond individual parts together, such as the Nitinol tubes (Figs. 5f and 5g), wire guide disks, and circular/half-circular disk (Figs. 5h and 5i). The FBG sensors

and Nitinol tubes (Fig. 5g) were also fixed by the bonding method. The structure of the actuation unit was manufactured by 3D printing. For cleaning and sterilisation purposes, the flexible insertion unit can easily be separated from the actuation unit.

Visualization and Image Mosaicking

A custom confocal laser endomicroscopy system (Thorlabs USA) with a leached fibre bundle (Schott North America, Inc.) was employed to acquire the micro images in this study. The flexible fibre bundle is approximately 1000 mm in length, containing 11000 cores. The leached fibre bundle is much more flexible than fused bundles, which enables the use of the full bending motion range of the tip. The context-weighted correlation ratio (CWCR)-based mosaicking method[8] was utilised to reconstruct pCLE videos, in which a feature matching strategy first tracked the inter-frame shift and then refined the result by template matching. To ensure the mosaicking accuracy, the CWCR metric that incorporates context information into intensity information was used to measure the differences between frames. For each newly read frame, once it is aligned to the reference space, it is inserted into the mosaic by the distance-weighted alpha blending strategy.

RESULTS

Calibration and Validation of Force Sensor

The experiments were conducted to calibrate the force sensor and validate the force calculation algorithms. The calibration setup is shown in Fig. 6a, which consists of a linear stage, two rotary stages, a precision scale, an FBG interrogator. The linear stage was used to generate the motion in the perpendicular direction and then change the magnitude of the applied force. To apply the force in different directions, the two rotary stages were employed to adjust the orientation of the force sensor. The deflection angle of the whole instrument and the rotation along its longitude axis are defined as β_Y and α_R, respectively (Fig. 6a). The actual X, Y, and Z components of the external force applied to the tool tip can be calculated as follows:

$$F = [F_x F_y F_z] = [F_S \cos \alpha \sin \beta \, F_S \sin \alpha \sin \beta \, - F_S \cos \beta] \qquad (8)$$

where F_S denotes the applied external tip force, which can be read from the scale. Seven angles β_Y and twelve angles α_R were combined to generate a total of 84 directions. The angle β_Y ranged from 0° to 90° with 15°
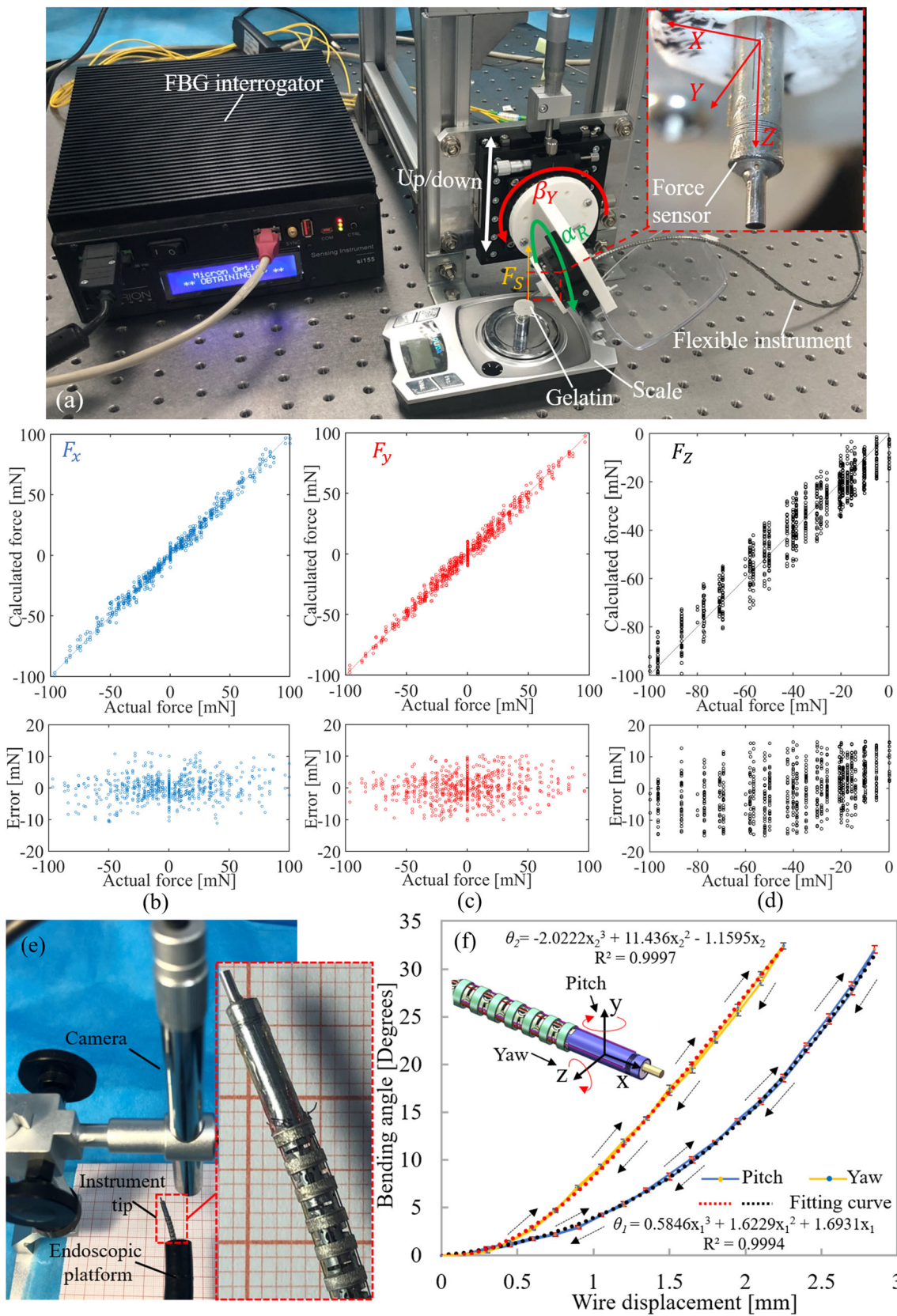
FIGURE 6. (a) Calibration setup. (b–d) The results of calibration and validation. (e) Experimental setup for wire displacement vs. bending angle. (f) Experimental results.

intervals, while the angle α_R ranged from 0° to 180° with 30° intervals. The force magnitude from 0 to 10 g in 2 g increments was applied three times for each angle combination. In total, 1260 samples were recorded. The slope k in Eq. (2) can be calculated experimentally. The instrument was maintained inside the laboratory for 5 h. During this procedure, the wavelength variations of the four FBG sensors were attributed to the changes in the environmental temperature. The results demonstrate that the wavelength variations of the four FBG sensors were almost the same. Consequently, the slope k defined in Eq. (2) is 1.

Using the linear model in "Force Calculation Algorithm" section to predict the lateral force, we found the best-fit pseudoinverse matrix using least-squares regression as

$$K_t = \begin{bmatrix} -2222.658 & 141.406 & 1416.064 \\ -2734.602 & 2861.601 & -1078.673 \end{bmatrix} \quad (9)$$

The wavelength resolution of the FBG interrogator reached 1 pm. With the coefficient matrix (9), the lateral force resolution is 2.8 mN.

To obtain the non-linear relationship between the axial force and the wavelength variations of the four FBG sensors, all the recorded data were used to train the proposed non-linear method in "Force Calculation Algorithm". Using the trained ANN model, we can predict the force when the wavelengths of the four FBG sensors are given as inputs. For the axial force, we used 1 pm as the input to the ANN model, and the axial force resolution can be derived with 4.6 mN.

Figures 6b–6d show the estimated force components F_x, F_y, and F_z versus their actual values as well as the residual errors. The estimation of all three force components is consistent with the actual values. The root-mean-square errors are 3.6, 3.9, and 6.9 mN for F_x, F_y, and F_z, respectively.

The validation experiments indicate that the 3-DOF force-sensing unit can provide precise measurements for a random spatial force with the desired resolution and accuracy.

Statistical Kinematics

In this experiment, the motion of the flexible instrument tip was captured by a calibrated camera (A1, 1920 × 1080 pixels, ANDONSTAR Inc., China) (Fig. 6e). The instrument was actuated from a straight state to 30° and vice versa in two orthogonal bending directions (wire displacement increment: 0.15 mm). The bending angle range (0–15°) was sufficient to scan a 3 mm^2 area. Each test was repeated three times, and the results were averaged. As shown in Fig. 6f, the hysteresis between the actuation and return stroke is

minimal. In the two bending directions, the bending behaviours are inconsistent; hence, two motion laws were used to control the two orthogonal bending modes of the manipulator. A non-linear relationship can be observed between the bending angle and the displacement of the actuation wires. The results show that the manipulator can be precisely controlled to achieve a raster trajectory.

Scanning Trajectory Evaluation

An NDI Aurora electromagnetic tracking system (6 DOFs sensor, positioning accuracy RMS: 0.48 mm, NDI Corp., USA) was used to evaluate the scanning trajectory of the instrument, as shown in Fig. 7a. A miniaturised electromagnetic sensor (6-DOF) was fixed on the distal end of the force sensor unit. The flexible instrument was inserted into the working channel of a simple 3D-printed endoscopic platform. The length from the tip of the instrument to the edge of the working channel is approximately 24 mm. Then, raster trajectory scans were performed three times with an average tangential velocity of 0.5 mm/s. We randomly chose one set of data to evaluate the raster trajectory.

The 3D and 2D trajectories are illustrated in Figs. 7b and 7c. The experimental results demonstrate that the flexible instrument can achieve the desired raster trajectory (4 mm × 3 mm in the 2D plane) with a positioning error of less than 0.5 mm.

Scanning and Mosaicking Validation

To evaluate the scanning and mosaicking performance of the flexible instrument, we performed scanning experiments with freshly excised porcine gastric tissue stained with acriflavine.

The instrument was inserted through the working channel of the 3D-printed model endoscopic platform (Fig. 8a). Before scanning, the instrument was actuated along its axis to make contact with the stained tissue. The pure axial contact force is linear with the variation of the Δs_4; therefore, we can find the proper initial contact force. This proper initial contact force was obtained empirically by actual imaging experiments (range: 20–40 mN).

The space between adjacent scanning centre lines was set as 0.35 mm to ensure sufficient overlap. The scanning arc length of reciprocating motion, and the average tangential velocity of the probe were approximately 2.2 mm and 0.26 mm/s, respectively. Because of the existing overlap, the target scanning area is approximately 5.1 mm^2. Five sets of scanning experiments were conducted with raster trajectory, two of which were chosen randomly for mosaicking evaluation. Figures 8b and 8c show the mosaicking results,
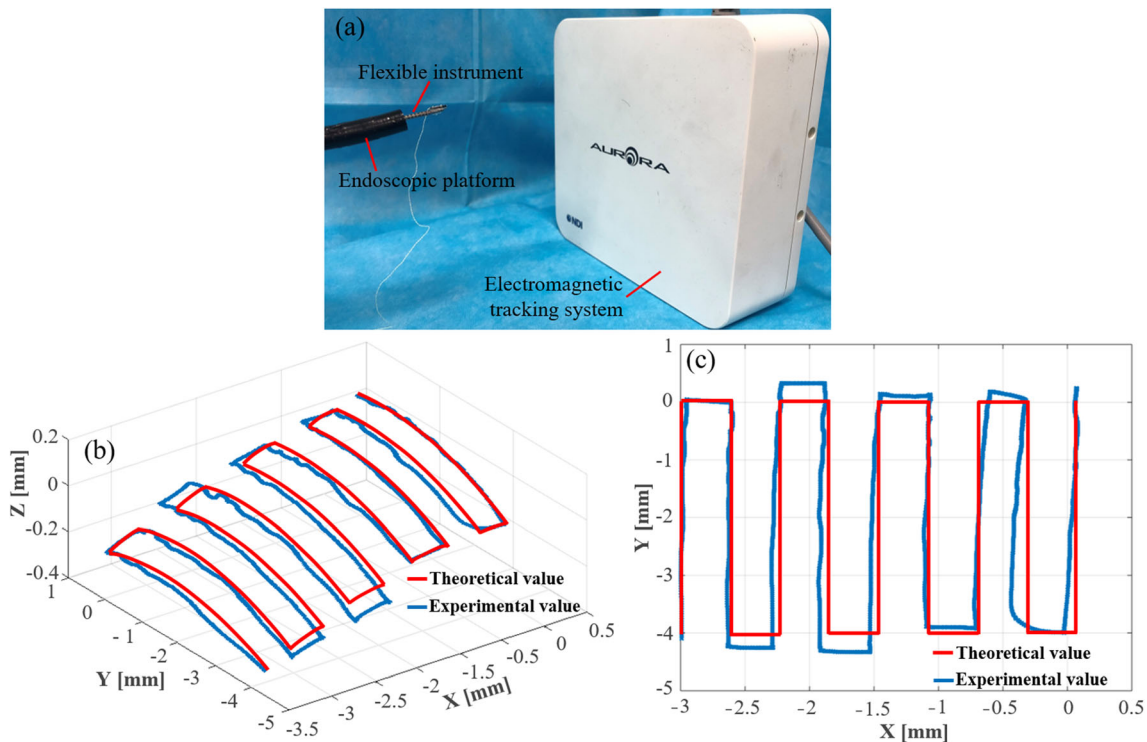
FIGURE 7. (a) Experimental setup. (b) 3D raster trajectory. (c) 2D raster trajectory.

which cover an area of approximately 4.4 and 3 mm^2, respectively. The scanning time was approximately 1 minute, as shown in Fig. 5c. The key morphological features of porcine gastric tissue can be observed from mosaicking. The prominent features are adipocytes and polygonal-shaped crypt cells. The force variation tendency is roughly similar for five raster scans. We chose one of them to show the result of contact forces (Fig. 8d). These data demonstrate that the contact force (Z-component) changed in the range of 0 to − 40 mN. The range of the contact force (X/Y-component) was − 25 to 40 mN. The component force along the X and Y axes changed periodically; however, this feature was not significant along the Z-component. The three-component forces along the X-, Y-, and Z-axes decreases gradually with the increase in deflection angle.

DISCUSSION

In this study, we developed a novel flexible scanning instrument integrated with FBG-based 3-DOF force sensing for gastric endomicroscopy. The flexible instrument is extremely compact (2.7 mm in diameter) and can be used with most endoscopic platforms. The developed instrument achieved a local microscopic panoramic image of stomach tissue up to 4.4 mm^2.

Experiments were conducted to calibrate the force sensor and validate the force-sensing performance. The

differential mode method was found to be effective in removing the influence of temperature. The eccentric configuration of the imaging probe and the centre FBG remains a compromise design to measure the spatial 3-DOF force. In the future, a new configuration method for FBG sensors should be developed without occupying the centre of the working channel.

The contact-aided compliant mechanism can improve the tensile and torsional strength. However, the slit between contact-aided structures is approximately 20 μm, and incomplete blanking may occur in the manufacturing process. The cost of the Nitinol tube may be decreased by mass production. The material composition of the Nitinol can affect the phase transformation temperature A_f (the Austenite finished temperature). When the temperature is higher than the A_f, the stress-induced martensite phase transformation happens under the external force or moment and when the applied stress is removed, the material returns to its original shape (i.e., Nitinol present super-elasticity behaviour).[4] The characteristic reports of the used Nitinol tube from the factory show that the A_f is 1 °C. Thus, this instrument can fully present the super elasticity of the material at room and operation temperature (such as body temperature 37 °C) during bending motions. Stiffness is a key parameter in the design of compliant mechanisms that affect the force output and stability. In this study, emphasis is placed on the
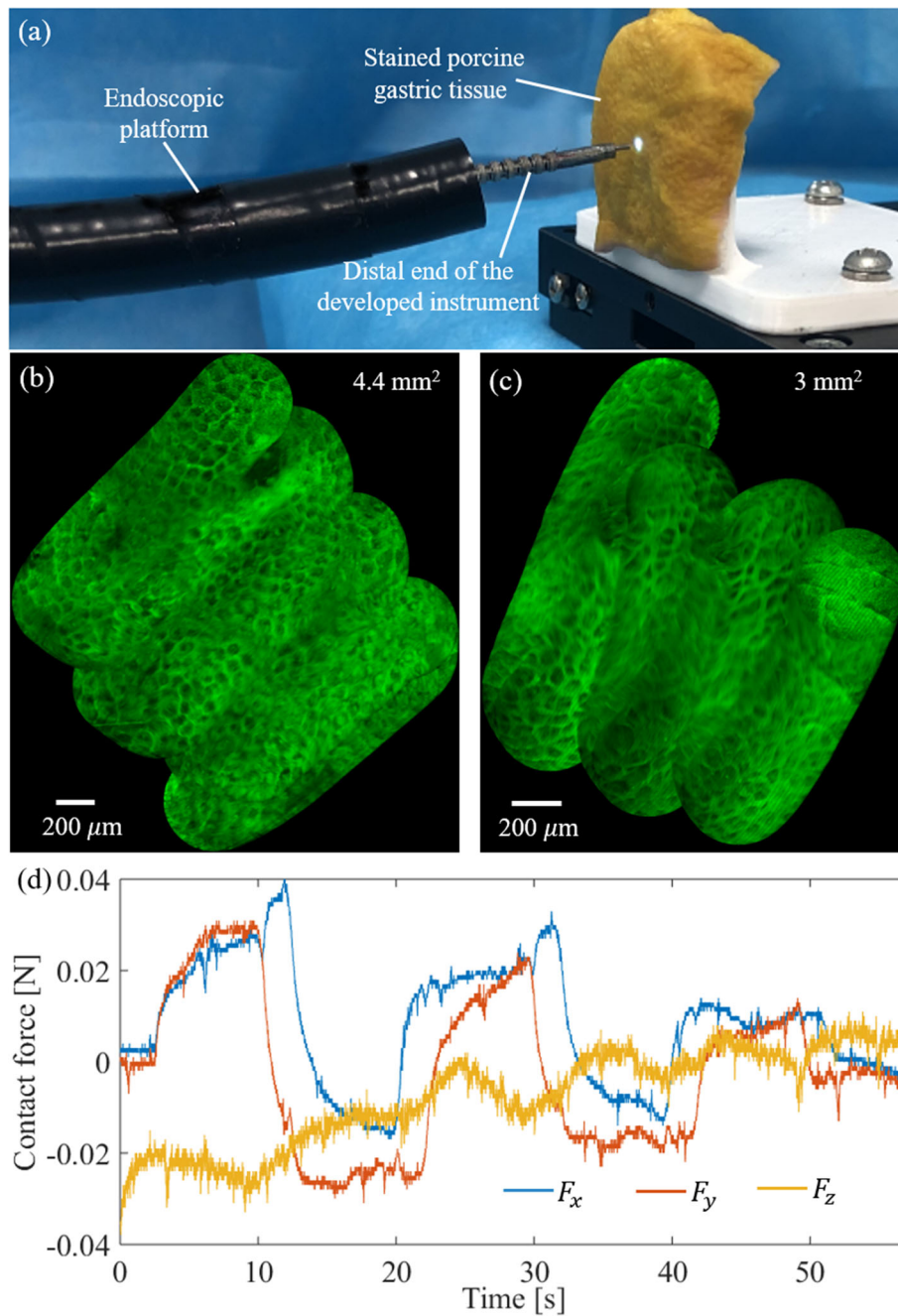
FIGURE 8. (a) The experimental setup. (b–c) Porcine gastric tissue mosaic images. (d) Force variation during the scanning process.

architecture of a complete system. Hence, optimisation of the structure should be achieved in future work. To acquire high-resolution motion control, a statistical method was employed to improve the motion accuracy. Trajectory evaluation experiments demonstrate that the statistical kinematics-based method can predict the motion precisely. The flexible instrument can achieve a raster trajectory, and the positioning accuracy reached 0.5 mm when the bending angle is small

($\pm$ 15°). A large deflection angle can cause cumulative errors and change the position of the focal plane. Both factors affect the mosaicking quality. Although the position errors are approaching the resolution (RMS: 0.48 mm) of the electromagnetic tracking sensor, the experimental results of gapless mosaicking (centreline spacing between two adjacent scanning is less than 0.5 mm) also verified the accuracy of the instrument.

The proposed flexible instrument achieved a mosaicking area of 4.4 mm^2. It took approximately 1 minute to scan the target surface, as shown in Fig. 8b. The efficiency is higher than that of traditional imaging methods, such as frozen section (40 min) and X-rays (more than 5 min). In fact, the area in conventional pinch biopsy is typically less than a 2 mm × 2 mm; hence, it satisfies the clinical requirements. Previous studies[6,7] were aimed at generating a gapless mosaic of 3 mm^2 using a rigid device. The flexible instrument in this work provides an increased coverage area compared with a rigid device. The *in vivo* experiments will be performed to further verify the performance of the proposed instrument in future.

Force adaptive control is helpful for scanning in this type of flexible instrument. In previous rigid scanning devices,[16,25] closed-loop control was developed to assist in scanning. However, existing methods are difficult to apply directly. Hysteresis results from the friction between the instrument and working channel of the endoscopic platform and the deformation of compliant mechanisms are the main factors that make axial motion difficult to achieve smoothly and precisely. Therefore, such small-dimension force adaptive control is challenging.

The proposed flexible instrument can potentially be extended to other surgical applications that requires both central channel and force sensing, such as cannula for intracerebral hemorrhage evacuation, surgical devices (forceps, electric surgical knives, laser ablation fibres, *etc.*) for endoscopic procedure, catheter for cardiovascular procedure and ophthalmic surgical tools.

ACKNOWLEDGMENTS

REFERENCES

[1]Balicki, M., A. Uneri, I. Iordachita, J. Handa, P. Gehlbach, and R. Taylor. Micro-force sensing in robot assisted membrane peeling for vitreoretinal surgery. In: *International Conference on Medical Image Computing and Computer-Assisted Intervention*, 2010, pp. 303–310.

[2]Bray, F., J. Ferlay, I. Soerjomataram, R. L. Siegel, L. A. Torre, and A. Jemal. Global cancer statistics 2018: GLOBOCAN estimates of incidence and mortality worldwide for 36 cancers in 185 countries. *CA. Cancer J. Clin.* 68(6):394–424, 2018.

[3]Burgner-Kahrs, J., D. C. Rucker, and H. Choset. Continuum robots for medical applications: a survey. *IEEE Trans. Robot.* 31(6):1261–1280, 2015.

[4]Chekotu, J. C., R. Groarke, K. O'Toole, and D. Brabazon. Advances in selective laser melting of nitinol shape memory alloy part production. *Materials.* 12(5):809, 2019.

[5]Cutsem, E. V., X. Sagaert, B. Topal, K. Haustermans, and H. Prenen. Gastric cancer. *Lancet.* 388(10060):2654–2664, 2016.

[6]Erden, M. S., B. Rosa, N. Boularot, B. Gayet, G. Morel, and J. Szewczyk. Conic-Spiraleur: a miniature distal scanner for confocal microlaparoscope. *IEEE/ASME Trans. Mechatron.* 19(6):1786–1798, 2014.

[7]Giataganas, P., M. Hughes, C. J. Payne, P. Wisanuvej, B. Temelkuran, and G. Z. Yang. Intraoperative robotic-assisted large-area high-speed microscopic imaging and intervention. *IEEE Trans. Biomed. Eng.* 66(1):208–216, 2019.

[8]Gong, L., J. Zheng, Z. Ping, Y. Wang, and S. Zuo. Robust mosaicing of endomicroscopic videos via context-weighted correlation ratio. *IEEE Trans. Biomed. Eng.* 2020. https://doi.org/10.1109/TBME.2020.3007768.

[9]He, X., J. Handa, T., P. Gehlbach, R. Taylor, and I. Iordachita. A Submillimetric 3-DOF force sensing instrument with integrated fiber bragg grating for retinal microsurgery. *IEEE Trans. Biomed. Eng.* 61(2):522–534, 2014.

[10]Hong, W., L. Xie, J. Liu, Y. Sun, K. Li, and H. Wang. Development of a novel continuum robotic system for maxillary sinus surgery. *IEEE/ASME Trans. Mechatron.* 23(3):1226–1237, 2018.

[11]Kitabatake, S., Y. Niwa, R. Miyahara, A. Ohashi, T. Matsuura, Y. Iguchi, Y. Shimoyama, T. Nagasaka, O. Maeda, T. Ando, N. Ohmiya, A. Itoh, Y. Hirooka, and H. Goto. Confocal endomicroscopy for the diagnosis of gastric cancer in vivo. *Endoscopy.* 38(11):1110–1114, 2006.

[12]Kutzer, M. D. M., S. M. Segreti, C. Y. Brown, R. H. Taylor, M. Armand and S. C. Mears. Design of a new cable-driven manipulator with a large open lumen: Preliminary applications in the minimally-invasive removal of osteolysis. In: *IEEE International Conference on Robotics and Automation*, 2011, pp. 2913–2920.

[13]Latt, W. T., R. C. Newton, M. Visentini-Scarzanella, C. J. Payne, D. P. Noonan, J. Shang, and G. Z. Yang. A handheld instrument to maintain steady tissue contact during probe-based confocal laser endomicroscopy. *IEEE Trans. Biomed. Eng.* 58(9):2694–2703, 2011.

[14]Liu, J., B. Hall, M. Frecker, and E. W. Reutzel. Compliant articulation structure using superelastic NiTiNOL. *Smart Mater. Struct.* 22(9):2013.

[15]Luo, M., and L. Li. Clinical utility of miniprobe endoscopic ultrasonography for prediction of invasion depth of early gastric cancer: a meta-analysis of diagnostic test from PRISMA guideline. *Medicine.* 98(6):2019.

[16]Miyashita, K., T. O. Vrielink, and G. Mylonas. A cable-driven parallel manipulator with force sensing capabilities for high-accuracy tissue endomicroscopy. *Int. J. Comput. Assist. Radiol.* 13(5):659–669, 2018.

[17]Newton, R. C., S. V. Kemp, G. Z. Yang, D. Ellson, A. Darzi, and P. Shah. Imaging parenchymal lung diseases with confocal endomicroscopy. *Respir. Med.* 106(1):127–137, 2012.

[18]Schmitz, A., Shen. T, P. Berthet-Rayne, and G. Z. Yang. A rolling-tip flexible instrument for minimally invasive sur-

gery. In: *IEEE International Conference on Robotics and Automation*, 2019, pp. 379–385.

[19]Sonn, G. A., S.-N. E. Jones, T. V. Tarin, C. B. Du, K. E. Mach, K. C. Jensen, and J. C. Liao. Optical biopsy of human bladder neoplasia with in vivo confocal laser endomicroscopy. *J. Urol.* 182(4):1299–1305, 2009.

[20]Takahisa, T., I. Okumura, H. Kose, K. Takagiet, and N. Hata. Tendon-driven continuum robot for neuroendoscopy: validation of extended kinematic mapping for hysteresis operation. *Int. J. Comput. Assist. Radiol.* 11(4):589–602, 2016.

[21]Thompson, C. C., M. Ryou, N. J. Soper, E. S. Hungess, R. I. Rothstein, and L. L. Swanstrom. Evaluation of a manually driven, multitasking platform for complex endoluminal and natural orifice transluminal endoscopic surgery applications. *Gastrointestinal Endoscopy.* 70(1):121–125, 2009.

[22]Vercauteren, T., A. Meining, F. Lacombe, and A. Perchant. Real time autonomous video image registration for endomicroscopy: fighting the compromises. *Biomed. Opt.* 6861:68610C, 2008.

[23]Wallace, M. B., G. Y. Lauwers, Y. Chen, E. Dekker, P. Fockens, P. Sharma, and A. Meining. Miami classification for probe-based confocal laser endomicroscopy. *Endoscopy.* 43(10):882–891, 2011.

[24]Wang, H., S. Wang, J. Li, and S. Zuo. Robotic scanning device for intraoperative thyroid gland endomicroscopy. *Ann. Biomed. Eng.* 46(4):543–554, 2018.

[25]Wisanuvej, P., P. Giataganas, K. Leibrandt, J. Liu, M. Hughes, and G. Z. Yang. Three-dimensional robotic-assisted endomicroscopy with a force adaptive robotic arm. In: *IEEE International Conference on Robotics and Automation*, 2017, pp. 2379–2384.

[26]York, P. A., P. J. Swaney, H. B. Gilbert, and R. J. Webster III. A Wrist for Needle-Sized Surgical Robots. In: *IEEE International Conference on Robotics and Automation*, 2015, pp. 2964–2970.

[27]Zorn, L., F. Nageotte, P. Zanne, A. Legner, B. Dallemagne, J. Marescaux, and M. Mathelin. A novel telemanipulated robotic assistant for surgical endoscopy: preclinical application to esd. *IEEE Trans. Biomed. Eng.* 65(4):797–808, 2018.

[28]Zuo, S., M. Hughes, C. Seneci, T. P. Chang, and G. Z. Yang. Towards intraoperative breast endomicroscopy with a novel surface scanning device. *IEEE Trans. Biomed. Eng.* 62(12):2941–2952, 2015.